Evaluation of the Performance Characteristics of the PC 4600 Positron Emission Tomograph

K. J. Kearfott and L. R. Carroll

Abstract: The sensitivity, resolution, linearity, and count rate capability for the PC 4600 positron emission tomograph (PET), a neurological PET with five rings of 96 bismuth germanate crystals, are reported along with details of the design of this system. Phantom studies and preliminary human images demonstrate the clinical potential of this new instrument. **Index Terms:** Emission computed tomography, apparatus and equipment—Phantoms—Bismuth germanate—Emission computed tomography.

Positron emission tomography (PET) is a powerful noninvasive imaging technique which permits the regional measurement of biochemical processes *in vivo*. Positron emission tomography instrumentation has improved steadily since the first medical image was performed with positron emitters in 1953 (1). A diverse array of clinically useful PET devices currently exists (2–16). This work reports the results of a performance evaluation of the Cyclotron Corporation Model PC 4600 Neuro-PET, the development of which has been discussed elsewhere (17). A discussion of sensitivity, resolution, and count rate is included.

SYSTEM DESIGN

Detectors and System Geometry

The PC 4600, shown in Fig. 1, consists of five rings of 96 bismuth germanate crystals (1.9 cm diameter × 3.8 cm deep) sheathed in 0.6 mm thick lead on a 60 cm (front-face-to-front-face) diameter circle. Each crystal, with its corresponding photomultiplier tube, timing discriminator, and dual-threshold energy discriminator, views 21 opposing crystals in its own ring and 21 crystals in each adjacent ring. Crystals in adjacent rings are offset by one-half the detector spacing.

Rings are separated by 3 mm thick, 13 cm deep shielding tungsten-alloy septa which permit the nearest neighbor cross-plane ray to be recorded. A total of five straight-across plane and four cross-plane tomographic slices are possible. The patient port is 28.5 cm in diameter and a fixed external 2.5 cm thick lead collar is provided to block the patient's body from radiation. The total axial field of view is 11.2 cm without axial sampling, which may be performed by computer-controlled couch motion if desired.

Front-end Electronics

Each ring of detectors is organized into eight groups of 12 for each coincidence plane, with each group in coincidence with three opposing groups in the same and each adjacent ring. Each group-to-group coincidence relationship is termed a superchord. There are 12 superchords (hence 12 coincidence gates) per plane and 13 coincidence planes (five straight-across planes plus four times two cross-planes) for a total of 156 coincidence gates for the whole system of five rings.

Each detector channel has its own dual-threshold energy discriminator in which the lower and upper energy thresholds are fixed at 300 and 700 keV, respectively. The amplitude of the scintillation pulses for each detector may be adjusted in a few minutes prior to each operating period using special software controlling the amplifiers and the built-in ^{68}Ge/^{68}Ga rod source to center the photopeak between the thresholds.

Timing performance with bismuth germanate is limited by the small number of photoelectrons per

From the Department of Neurology, Memorial Sloan-Kettering Cancer Center, New York, NY (K. J. Kearfott), and the Cyclotron Corporation, Berkeley, CA (L. R. Carroll). Address correspondence and reprint requests to Dr. Kearfott at Department of Neurology, Memorial Sloan-Kettering Cancer Center, 1275 York Avenue, New York, NY 10021.
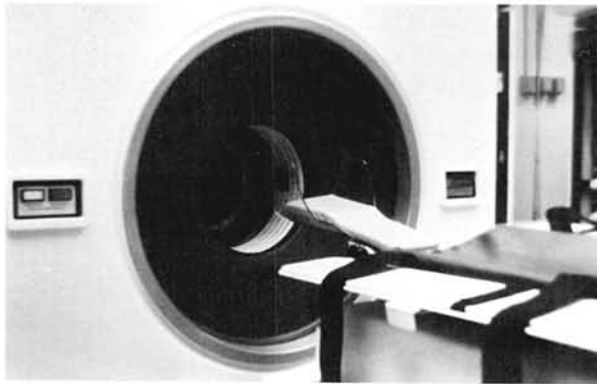
FIG. 1. The PC 4600 Neuro-PET (cosmetic shield not in place).

scintillation. Each 511 keV phototube impulse has a leading edge comprising only a few electrons per nanosecond at the photocathode. Acceptable timing resolution, however, may be obtained by employing leading edge discrimination and triggering at very low levels (preferably in the first photoelectron "swarm"). A special noise-rejection scheme is included in each discriminator circuit to minimize the contribution of single quantum excitation and "dark current" events to coincidence deadtime. Every event, whether due to a burst of noise or a valid scintillation event, trips a single-shot multivibrator of 30 ns duration. A comparator circuit verifies that the signal triggering the pulse is still present at the end of the 30 ns. If the signal is still present, a timing pulse issues from the discriminator; otherwise, no timing pulse is generated.

Deadtime

Whenever a coincidence event is recorded, all the superchords associated with the detector groups involved (including inter-ring and intra-ring superchords) are "blanked" during the nominally 1–2 μs interval required to process the coincidence. This blanking of 16 additional superchords for every superchord in which an event actually occurred is the major source of system deadtime. Although the cross-plane coincidence capability more than doubles system sensitivity, it compounds system deadtime. Compensation for deadtime is performed at reconstruction time by increasing the observed count rates, R, by a factor $e^{17R\tau}$, where τ is the equivalent deadtime per coincidence event (determined experimentally as approximately 1 μs).

Sampling

The intrinsic spatial resolution of a coincidence pair is of the order of one-half the aperture of a single detector. To realize full resolution, the sampling rate must be at least twice the highest frequency component contained in the line spread function (LSF). A 1 cm full width at half maximum (FWHM) (assuming a gaussian LSF) thus requires two samples per centimeter minimum sampling rate. In practice, a higher rate is usually required. The PC 4600 uses four samples per centimeter.

To increase the density of spatial sampling, the entire array of detectors is moved continuously in a circular orbit (17 mm diameter, for a 24 cm field of view) at a rate of 12 wobbles/min, while depositing data into small "bins." The distance between each detector chord (2 cm) is divided into eight uniformly spaced bins, each 2.5 mm wide. The sampling, or bin spacing, is uniform whereas the dwell time of the system at each bin varies. This results in a systematic variation in bin-to-bin sensitivity, which is corrected in software during subsequent image reconstruction.

For more rapid studies at low resolution, rotation at one crystal spacing per second, with sampling every half crystal spacing (for a total of four crystal spacings in either direction), is possible. Ultrarapid studies (22 cm field of view) may be conducted without ring motion.

Randoms Correction

Random coincidence correction for emission scans may be performed using known resolving times and singles rates, which are recorded for each channel during data collection. A detector pair-by-pair randoms estimate is calculated using the formula $R_r = 2\tau_R S_1 S_2$, where S_1, S_2 are singles rates in each detector and $2\tau_R$ is the resolving time, nominally 20 ns.

Scatter Correction

Problems of scatter and scatter correction as related to PET have been discussed by several authors (18–20). The PC 4600 detector diameter and shielding configuration were designed for optimum effective count rate: the best compromise between sensitivity for true events and acceptance of unwanted background (17). The system software includes provision for scatter correction by using a scatter deconvolution kernel incorporated into the reconstruction filter.

Computer System

Data are acquired through a set of stand-alone, dual-buffered memories, which transfer data onto the main system disc. The system is controlled by a PDP 11/60 with a 67 Mbyte RM02 and two RL01 disc drive units. An Analogic AP400 array processor and a floating point accelerator facilitate image reconstruction. All data acquisition, reconstruction, and image processing software are modular, menu-driven, and user-oriented.

Orbiting Rod Source

An orbiting rod source (ORS) is included with the PC 4600 to provide a means of automatically adjusting energy thresholds (see above), gathering transmission data for attenuation corrections, and correcting for detector nonuniformity (inhomogeneity) (21). Attenuation data may be obtained by taking the ratio of data obtained when the rod source is rotated about an empty port and data obtained with the object in place. Relative count rates from the empty-port scan with the ORS may also be used to normalize for differences in individual detector pair sensitivities. This 10 mCi ^{68}Ge source has a length of 13 cm and is encapsulated in 3.2 mm outside diameter (<1 mm thick) nickel tubing. The use of such a source simplifies storage, shielding, and handling as compared with the more often used ring or hoop source. Computer-driven motors are used to extend the source into the camera and rotate it about the port (just outside the field of view) or to retract it into a 4 inch diameter lead-shielded storage area within the gantry assembly.

For a given source strength, peak count rates (at detectors nearest the source's current position) are higher with the ORS than with a conventional ring or hoop source (in which activity is distributed uniformly around the ring). However, for this particular tomograph geometry, random coincidence count rates (which depend on the sum of the instantaneous products of photon count rates in opposing detectors) are actually lower for the ORS than for the corresponding equivalent hoop source. Moreover, knowledge of the source position may be used to reject randoms on a count-by-count basis. Such an approach avoids the degradation in signal-to-noise ratio associated with random coincidence correction techniques that use an estimate of mean randoms rate using delayed coincidences or singles counting.

Correction for ORS random coincidences is accomplished using an on-the-fly "rod source masking" technique to reject most randoms. The masking algorithm accepts only those coincidences occurring on chords within a given acceptance angle set by the source position. The arc may be large relative to the source although still removing most randoms, thus permitting a reasonable computation time. Any "residual" randoms that are not masked out may be estimated and subtracted from the data using a singles counting technique. A practical acceptance arc of 36° is currently being used.

METHODS

Sensitivity

System sensitivity was measured using a 20 cm diameter, 5 cm long, water-filled phantom with 0.4 mm thick walls filled with 0.13–0.17 μCi/ml ^{18}F so-

lution. Prompt coincidence counts (no attenuation correction) for 5 min low and high resolution studies were corrected for positron abundance per decay and for decay during the measurement period.

Transverse Resolution

The measured FWHM depends on the scattering medium surrounding the line source, the material of the source container, and positron energy (22,23). Measurements were performed by imaging 18, 19, 20, 22, and 25 gauge stainless steel spinal needles and 20 gauge Teflon tubing inserted at positions varying from the center to the outside of a solid, 20 cm diameter Lucite phantom. Analytic attenuation corrections and detector inhomogeneity corrections were performed. For high resolution data a 128 × 128 reconstruction matrix was employed using an unweighted ramp reconstruction filter with a 1.4 cycle/cm cutoff frequency. For non-wobbled studies a 0.5 cycle/cm cutoff frequency was used with a 64 × 64 reconstruction matrix. Care was taken to align the sources coaxially in the tomograph, to avoid air bubbles in the needles, and to obtain adequate counting statistics. Gaussian functions were fit to profiles running through the reconstructed points in the images using a nonlinear least squares fitting routine (24) to determine the FWHM. To study the effects of reconstruction filter on image resolution, the same data set was reconstructed using Shepp-Logan, ramp, and Hann-weighted filters with cutoff frequencies ranging from 0.5 to 2 cycles/cm.

Axial Resolution

The axial resolution of the PC 4600 Neuro-PET was determined by sandwiching a small ^{68}Ga source (0.5 × 0.5 cm, <3 mm thick) between two 20 cm diameter solid Lucite phantoms and moving this in 4 mm axial couch increments through the scanner port, recording total counts at each position. The experiment was repeated with the source at 0, 2, 4, 6, and 8 cm from the center of the phantoms. Gaussian functions were fit to determine the FWHM of the axial spread function. To determine an "average" slice thickness, a 20 cm diameter ^{68}Ga sheet source was also prepared and moved through the scanner port in 4 mm increments.

Count Rate Capability

Approximately 30 mCi of ^{68}Ga and, later, 90 mCi of ^{13}N were placed in a 17.8 cm diameter, 10 cm long vessel to study the performance of the tomograph at high count rates. A 17.8 cm diameter, 30 cm long vessel was used for additional experiments with 20–75 mCi ^{15}O, 80 mCi ^{11}C, and 95 mCi ^{13}N. Data were collected for at least three half-lives. The

results were corrected for randoms and deadtime, and the random-to-true coincidence ratio was determined as a function of count rate. The peak total count rate was observed for some studies; effective deadtime was estimated from the inverse of these data.

Linearity of Regional Quantitation

The linearity of regional quantitation was evaluated using methodology previously established (25). A 20 cm diameter phantom with five equal-volume sectors (pie phantom) was filled with calibrated activity concentrations of ^{68}Ga ranging from 0.1 to 7.0 μCi/ml. Data were collected for two half-lives. Analytic attenuation, random subtraction, inhomogeneity, and deadtime corrections were performed. Scatter correction was not performed. Regions of interest varying from 6 × 6 to 15 × 15 pixels (0.1875 cm/pixel) were chosen for the evaluation. A straight line was fit to the resulting counts per pixel as a function of activity concentrations, and the root mean square deviation of the data from this "best fit" straight line was determined.

Scatter

The contribution of scatter to the raw data was evaluated using the methods of Hoffman et al. (26). A 10 cm long, 17.8 cm (outside) diameter phantom was centered both axially and transversely in the port. Data were collected with activity in the central compartment, a single outer compartment, both outer compartments, and then in the center and one outer compartment. High resolution data for the central plane and neighboring cross-planes were obtained. The random/true ratio was <2% for the studies. Deadtime, inhomogeneity, and random corrections were applied to the raw data. Second-order polynomials were fit to the data lying along a line through the object center from one FWHM outside the physical boundaries of the object. The integrals of these functions were added together for the various experiments and compared with the total counts to provide a measure of the scatter.

Minimum Frame Rate

In high resolution mode the minimum collection time is one wobble orbit (5 s). To determine the minimum time required per frame in low-resolution mode, data for different numbers of planes were collected and the total time required to obtain eight frames was recorded.

Reconstruction Time

The time required to reconstruct a plane of data was recorded for various reconstruction matrix sizes with different corrections included.

Rod Transmission Source Evaluation

The count rate resulting from the orbiting rod source was determined for the empty tomograph port and for a 20 cm diameter water-filled vessel. To validate the masking software used for transmission attenuation correction data collection, data were obtained without rod source masking and random-corrected for comparison with masked data. The radiation dose to a patient was measured using lithium fluoride thermoluminescent detectors placed on the outside and in the center of a 20 cm diameter Lucite phantom.

A 20 cm diameter "donut" phantom filled with ^{68}Ga in solution but having a centrally placed 4.5 cm inside diameter (3 mm wall thickness) air-filled compartment was imaged. Transmission correction was performed using both analytic techniques and measured transmission data (15 min data collections for both empty-port and phantom scans). A 1.2/cm cutoff Hann-weighted ramp reconstruction filter was used to produce the images.

Instrument Shielding

Adequate shielding of the detectors from body activity outside the field of view is especially important for continuous inhalation studies using radiolabeled gases. A vial containing 6 mCi of ^{68}Ga (in 10 ml solution) was centered axially in the tomograph and moved 2.5, 15, and 30 cm from the center of the outermost detector ring to determine the adequacy of the PC 4600 shielding. The count rate in each plane for each position of this source was recorded and corrected for differences in interplane sensitivities. The experiment was performed both with and without a 17.8 cm diameter, 10 cm long water phantom centered in the port. The adequacy of the shielding of the retracted transmission source was tested by collecting data with no activity in the port and with other sources removed from the area.

Preliminary Imaging Studies

The Derenzo phantom (27) provides a good qualitative picture of the resolution capability of a PET instrument. This phantom, which consists of 2.5, 3.0, 3.5, 4.0, 5.0, and 6.25 mm diameter parallel holes in Lucite spaced by four times their diameters, was filled with a low concentration of ^{18}F to avoid the undesirable effects of randoms, supported by foam in the tomograph port, and imaged in the high resolution mode. A Hann-weighted ramp filter with a 1.2 cycles/cm cutoff frequency was employed for reconstruction.

A 20 cm diameter, 5 cm thick cold spot phantom was constructed with 6, 8, 10, and 12 mm diameter Lucite pegs distributed in four sectors and spaced by 2.5 times their diameters. In addition a sector with 4, 5, 6, 7, 8, and 9 mm diameter Lucite pegs

TABLE 1. *Effects of needle type and dimensions on measured image FWHM (cm)*

Needle gauge and type	Inside diameter (inches)	Wall thickness (inches)	Measured FWHM[a]
18 G SS[b]	0.034	0.0016	1.09 ± 0.06
19 G SS[b]	0.028	0.00145	1.06 ± 0.08
20 G SS[b]	0.0245	0.01125	1.06 ± 0.04
22 G SS[b]	0.017	0.01125	1.06 ± 0.03
25 G SS in 20 G SS[b]	0.010	0.0103	1.08 ± 0.02
20 G Teflon tubing	0.028	0.020	1.09 ± 0.04

[a] Average and standard deviation for 4 to 14 measurements of transverse resolution in straight-across planes made with ^{68}Ga positioned at center of a 20 cm diameter Lucite phantom.

[b] Becton-Dickinson stainless steel spinal needles.

spaced at 25 mm was included. This phantom was also imaged using ^{18}F and a 1.3 cycle/cm Shepp-Logan reconstruction filter.

The dynamic capabilities of the PC 4600 were demonstrated by obtaining 30 s images during the first 6 min of continuous inhalation of 10 mCi/L of CO^{15}O at a rate of 400 ml/min by a normal human subject. A sequence of 5-min high resolution scans was collected for a total of 25 min at equilibrium. Reconstruction was performed with a 128 × 128 matrix and an unweighted 0.66/cm ramp filter. A small (1 × 9 × 1 cc) irregular region of gray matter was selected for analysis.

The thin, multislice capability of the instrument was employed following the bolus inhalation of 25 mCi of ^{11}CO by a normal human volunteer. The collection of 20 overlapping planes of data was made possible by computer-controlled axial couch motion during the study. Data were reconstructed with a 0.8/cm ramp filter.

RESULTS

Sensitivity

The straight-across plane sensitivity was measured to be 26 ± 2 total coincidence kcps/μCi/cc, whereas the cross-plane sensitivity was measured to be 39 ± 1 kcps/μCi/cc, where the error bars represent the standard deviation of the measurements for each plane with respect to these mean values. For scatter/true fractions of 17 and 21% (those reported below adjusted for a smaller diameter but longer phantom), these sensitivities are approximately equivalent to 22 and 32 true kcps/μCi/cc for straight-across planes and cross-planes. The total system sensitivity was measured to be 286 (true plus scattered coincidence) kcps/μCi/cc.

Transverse Resolution

Computer-fitting, interpolation using a hand calculator, and plotting of the point-spread functions produced the same resulting values of the transverse image FWHM for 22 cases tested. Interpolated and graphically determined FWHMs differed by an average of 3–4% from fitted values, with the differences ranging from 0.1 to 16%. As indicated by the data included in Table 1, the measured FWHM did not depend significantly on the inside diameter and wall thickness of the needles used to contain the source. The FWHMs measured using

TABLE 2. *Measured FWHM (cm) in transverse direction for wobbled, rotated, and stationary data acquisition modes[a]*

	Distance from phantom axis (cm)		
	0	8	10
High resolution mode[b]			
Straight-across planes	1.06 ± 0.02[d]	1.10 ± 0.03	1.16 ± 0.06
Cross-planes	1.09 ± 0.02	1.14 ± 0.03	1.13 ± 0.06
Rotation mode[c]			
Straight-across planes	1.43 ± 0.01	1.46 ± 0.05	—
Cross-planes	1.49 ± 0.03	1.49 ± 0.08	—
Stationary mode[c]			
Straight-across planes	1.58 ± 0.03	1.56 ± 0.06	1.59 ± 0.10
Cross-planes	1.56 ± 0.01	1.64 ± 0.13	1.59 ± 0.07

[a] Measured with 19 gauge stainless steel spinal tap needles.

[b] Measurements with ^{18}F.

[c] Measurements with ^{68}Ga.

[d] Error bars represent standard deviation for measurements made on separate planes.

TABLE 3. *Dependence of image resolution (FWHM, cm) on reconstruction filter type and cutoff frequency[a]*

Cutoff frequency (cm^{-1})	Shepp-Logan	Ramp	Hann
2.00	1.11	1.06	1.13
1.75	1.13	1.08	1.14
1.50	1.17	1.06	1.18
1.25	1.27	1.04	1.25
1.00	1.49	1.03	1.38
0.75	2.00	1.13	1.64
0.50	3.78	1.48	2.24

[a] Determined using ^{18}F in stainless steel spinal needle centered in 20 cm diameter Lucite phantom.

[18]F were not significantly lower than those measured using ^{68}Ga, presumably because the positron range effects are comparable to the uncertainties involved in the measurements (for 20 gauge Teflon tubing in the center of the solid Lucite phantom, the average FWHM for straight-across planes was 1.09 ± 0.04 cm with ^{68}Ga and 1.07 ± 0.04 cm for ^{18}F). The measured transverse resolution for wobbled, rotated, and stationary data acquisition modes is summarized in Table 2. The measured resolution varied less than approximately 1 mm over the field of view, with a resolution of approximately 1.1 and 1.5 cm possible for the high and low resolution modes. Rotation does not improve resolution significantly over the stationary mode; however, gantry rotation may be used to smooth out detector
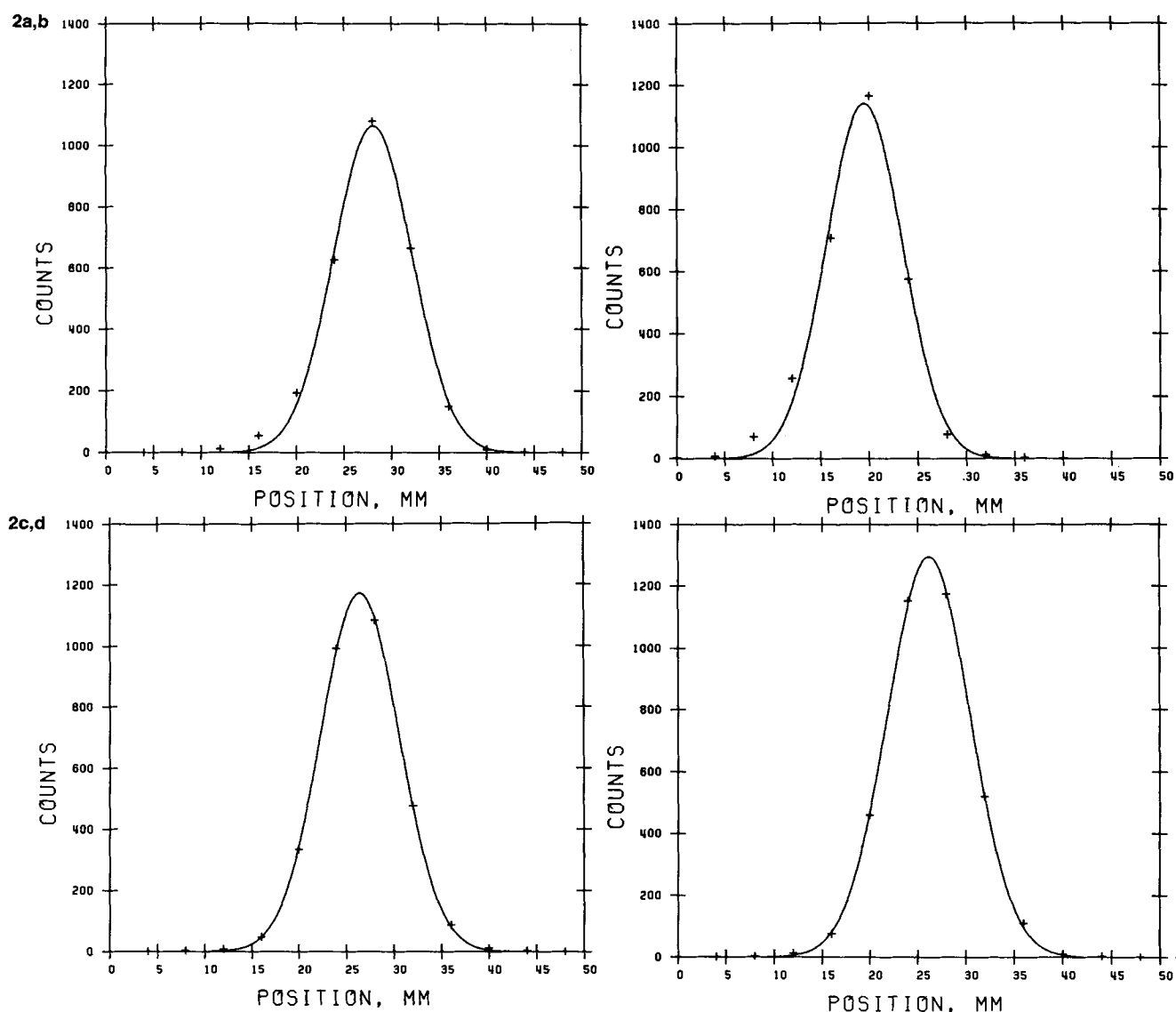

FIG. 2. Typical axial resolution line spread functions obtained using a point source at **(a)** the center of a straight-across plane (0.97 cm FWHM), **(b)** the center of a cross-plane (0.92 cm FWHM), **(c)** 8 cm from the center of a straight-across plane (1.00 cm FWHM), and **(d)** 8 cm from the center of a cross-plane (1.02 cm FWHM).
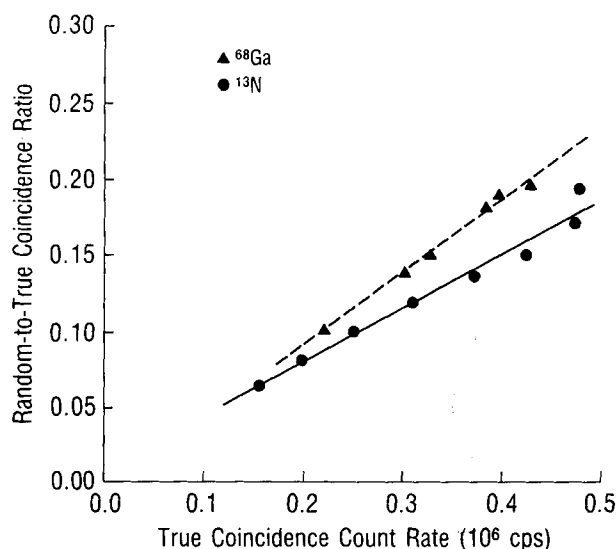
FIG. 3. Total system random-to-true coincidence ratio as a function of true coincidence count rate determined using ^{68}Ga and ^{13}N in a 17.8 cm diameter, 10 cm long phantom.
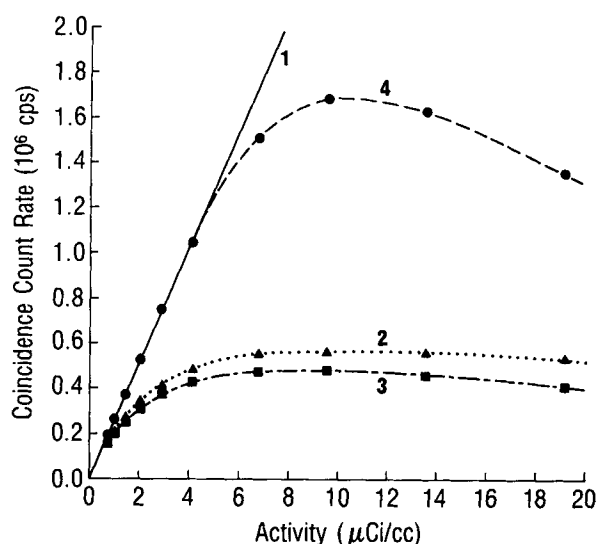

FIG. 4. Total system coincidence count rate as a function of activity concentration for [13]N. 1. Ideal linear behavior. 2. Raw coincidence counts. 3. Random-corrected (true) coincidence counts. 4. Random- and deadtime-corrected (true) counts.

inhomogeneities. The full width at tenth maximum ranged from 1.8 to 2.4 cm for the high resolution mode.

The dependence of resolution on reconstruction filter type and cutoff frequency is shown in Table 3 for Shepp-Logan, ramp, and Hann-weighted filters. Decreased resolution or smoothing occurs with decreasing cutoff frequency. Resolution with the ramp filters (which are prone to ringing artifacts) is less sensitive to the value of the cutoff frequency selected; noise in the measurements obscures the distinction between 1.0 and 2.0/cm ramp filters. In practice, images are smoothed to improve their appearance, which results in the loss of image resolution illustrated in Table 3.

Axial Resolution

Typical results obtained for axial resolution are shown in Fig. 2. Measurements of the axial resolution were observed to vary from 0.94 to 1.00 cm for straight-across slices. A notable consequence of the use of thin (3 mm) interplane septa is the excellent uniformity of axial resolution in the cross-planes: 0.83 to 1.02 cm FWHM, with resolution degrading measurably only near the edge of the field of view. The overall "average" slice thickness, determined using a sheet source, was observed to be 1.07 ± 0.04 and 0.93 ± 0.07 cm for the straight-across and cross-plane slices.

TABLE 4. *Results of high count rate studies*

Isotope	Initial mCi	(Random/true)/true, μs[a]		Peak kcps[a]		1/τ, μs[a]	
		Straight	Cross-plane	Straight	Cross-plane	Straight	Cross-plane
10 cm phantom							
[68]Ga	25	9.8 ± 11.2[a]	6.4 ± 6.5				
[13]N	90	3.7 ± 2.9	3.7 ± 2.3				
30 cm phantom							
[68]Ga	4	8.4 ± 1.8	9.8 ± 1.2				
[15]O	20	7.6 ± 1.7	7.7 ± 0.7				
[15]O	25	8.8 ± 1.7	10.6 ± 1.6				
[15]O	47	9.0 ± 1.9	10.1 ± 1.0				
[15]O	75	8.6 ± 1.1	10.2 ± 1.0	38 ± 3	57 ± 3	13.0 ± 0.9	8.8 ± 0.5
[11]C	81	6.2 ± 2.3	6.5 ± 1.0	43 ± 5	68 ± 6	11.7 ± 1.5	7.3 ± 0.6
[11]C	78	7.4 ± 0.9	8.7 ± 0.6	39 ± 3	58 ± 4	12.9 ± 1.2	8.6 ± 0.5
[13]N	96	8.7 ± 1.8	10.4 ± 1.4	37 ± 3	55 ± 3	13.6 ± 1.3	9.1 ± 0.6
Average for 30 cm phantom [b]		8.1 ± 1.0	9.3 ± 1.5	39 ± 3	60 ± 6	12.8 ± 0.8	8.5 ± 0.8

[a] Error bars are plane-to-plane standard deviation.
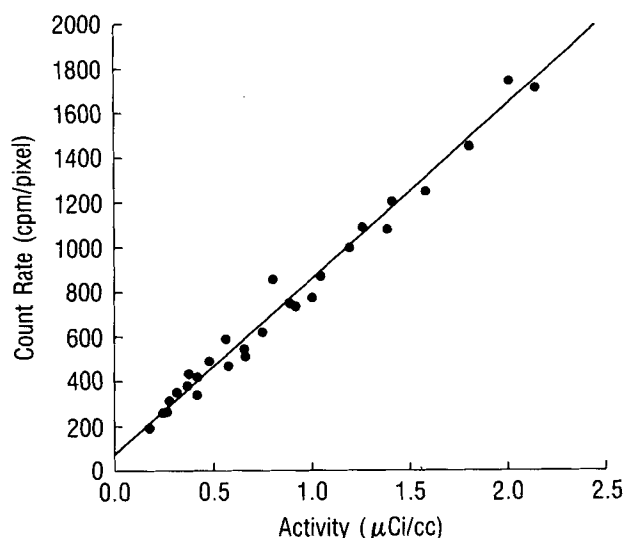[b] Error bars are experiment-to-experiment standard deviation.

FIG. 5. Linearity of response of PC 4600; data of 1.5 cc regions of interest are shown with a best fit straight line (r^2 = 0.993).

Randoms

Figure 3 shows the random-to-true coincidence ratio as a function of true coincidence rate for two of the high count rate studies. (No corrections for scatter were applied to these data.) Table 4, a summary of all high count rate experiments performed, includes the slopes of curves similar to those in Fig. 3. For the 10 cm long phantom, the random/true ratio was greater for centrally located planes and varied more plane-to-plane than for the 30 cm long phantom because of the decreased contributions due to scatter of extraplane activity in the outer planes. For a true count rate of 30 kcps/plane, the data reveal that the random-to-true ratio would remain less than approximately 25% for both straight-across planes and cross-planes. For ^{68}Ga, single photon emissions in the range of the 511 keV annihilations photons for this radioisotope (0.2% 580 keV, 0.45% 800 keV, 3.5% 1,080 keV, 0.15% 1,870 keV) should result in a somewhat increased randoms rate. This is apparent for the 10 cm long phantom but is obscured by noise in the measurements for the 30 cm long phantom.

Count Rate Capability

Observed peak count rates, summarized in Table 4 and determined using a 30 cm long phantom, ranged from 32 to 49 total kcps for straight-across planes and from 51 to 75 total kcps for cross-planes. Plane-to-plane variations in this count rate were greater than experiment-to-experiment variations. As illustrated by Fig. 4 (which shows total system count rates), the utility of the PC 4600 at extremely

high count rates is limited by deadtime and not by randoms rate. The data also show that when proper correction is made for deadtime, the scanner may be useful for quantitation for concentrations as high as approximately 4 μCi/cc (uniformly distributed in a 17.2 cm diameter object), which is seldom if ever encountered in clinical situations.

Linearity

The results of a typical linearity study appear in Fig. 5, where the counts/minute/pixel in a small (1.5 × 1.5 cm^3) region are plotted as a function of the activity concentration. For both straight-across planes and cross-planes, with regions of interest as small as 1 cc, the root mean square deviation of the data from the resulting best-fit straight line was less than 3.9%. The r^2 for such fits ranged from 0.98 to 0.993. Scatter correction was not included in this experiment. The effect of an uncorrected scatter component on quantitation can be inferred from the nonzero intercept of Fig. 5.

Scatter

Typical raw data profiles used for the Hoffman scatter measurement appear in Fig. 6. The scatter fraction, as determined using the Hoffman technique (expressed as scatter/true), was 15 ± 2% for the central straight-across plane and 18 ± 3% for the neighboring cross-planes for a 17.2 cm water-filled object (where the error bars represent the standard deviation for the measurements performed with different combinations of compartments).

Dynamic Capability

In low resolution (nonwobbled) mode 2.6 s is required to collect eight frames of all planes. If three straight-across planes are collected, only 1.02 s is needed. The average minimum data collection period was determined to be approximately 0.034 s/frame/plane, limited chiefly by disc data transfer rates.

Reconstruction Time

Image reconstruction requires 2.2, 2.9, and 5.1 s/plane for 32 × 32, 64 × 64, and 128 × 128 reconstruction matrices if all corrections (including inhomogeneity and attenuation) are performed, and approximately 1 s/plane less if corrections are not required. The ability to reconstruct images rapidly greatly facilitates patient throughput and image optimization.
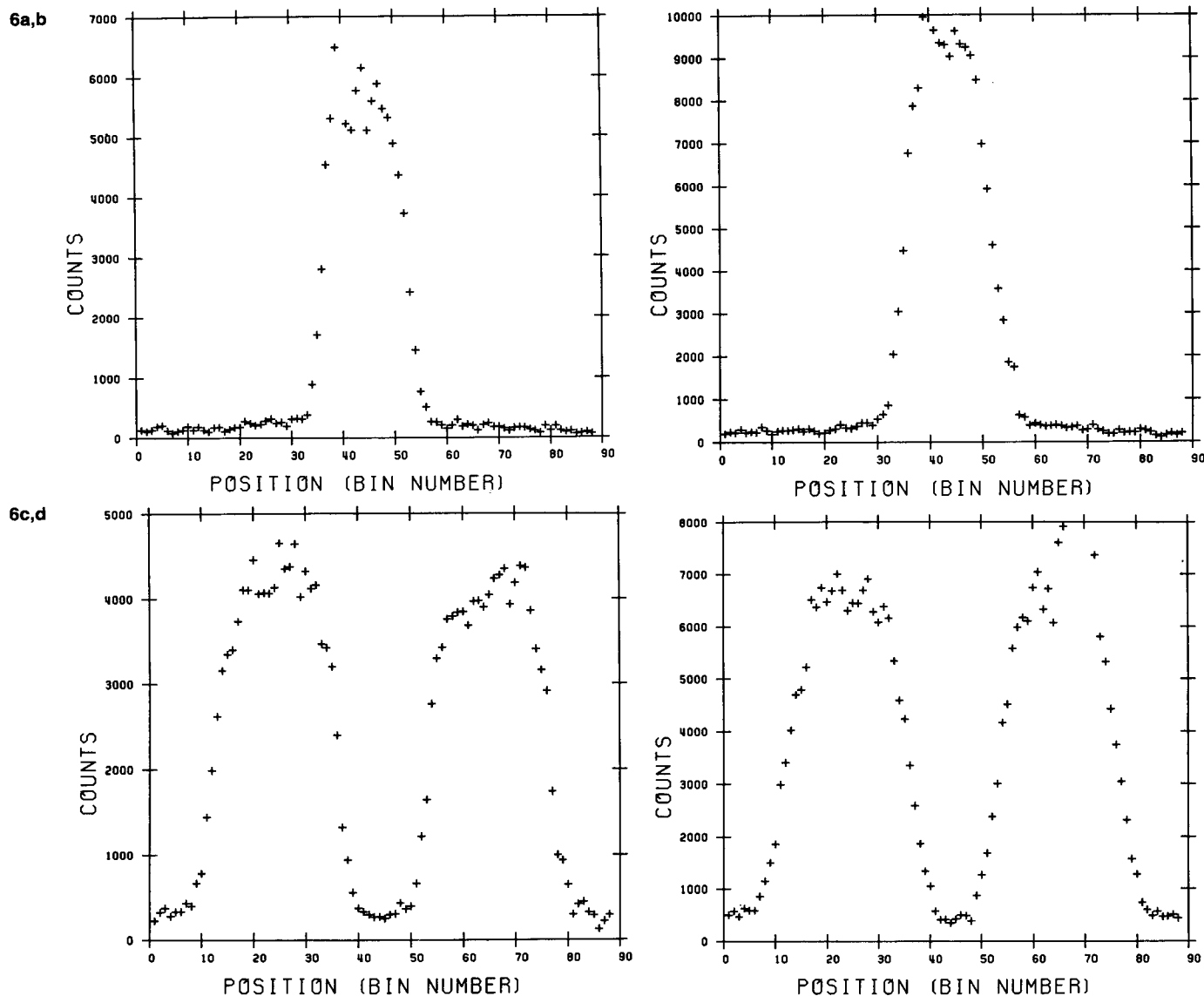
FIG. 6. Typical raw data profiles used for Hoffman scatter measurement with activity in central compartment of **(a)** straight-across plane and **(b)** cross-plane. Also shown are results for activity in both outer compartments of the phantom for **(c)** straight-across plane and **(d)** cross-plane. Each bin corresponds to approximately 0.27 cm.

Transmission Scans

The total system (nine slice) coincidence count rate was 334 kcps for an empty-port transmission scan with a 10 mCi source without masking. With a 17.2 cm diameter water-filled phantom, this count rate was 185 kcps. For 15 min transmission scans with the patient in place, approximately 167 million counts (18 million counts/slice) would thus be available. In patient studies, that is nominally an order of magnitude more counts than available for the corresponding emission scans, as is required for attenuation corrections. Masked transmission data differed from random-corrected unmasked data by only 0.5–8.6% (average difference for all planes was 4.9 ± 2.9%). The empty-port random/total was

14% with masking. The dose rate for transmission measurements was found to be 2.8 mrad/min at the surface and 1.5 mrad/min in the center of a 20 cm diameter Lucite object.

Images of the "donut" phantom, having a 4.5 cm air-filled cavity in the center, are included as Fig. 7. The empty-port and transmission scans resulted in 40 and 124 million counts, respectively (the ^{68}Ge/^{68}Ga rod source had decayed to 75% of its original strength). Approximately 110 million raw counts were available for the emission scans. As clearly illustrated in Fig. 7b, analytic attenuation correction for this type of object resulted in a misleading image. The cold (activity-free) air spot appears as a hot (activity-rich) region, since the correction assumes that water is present in the area although a
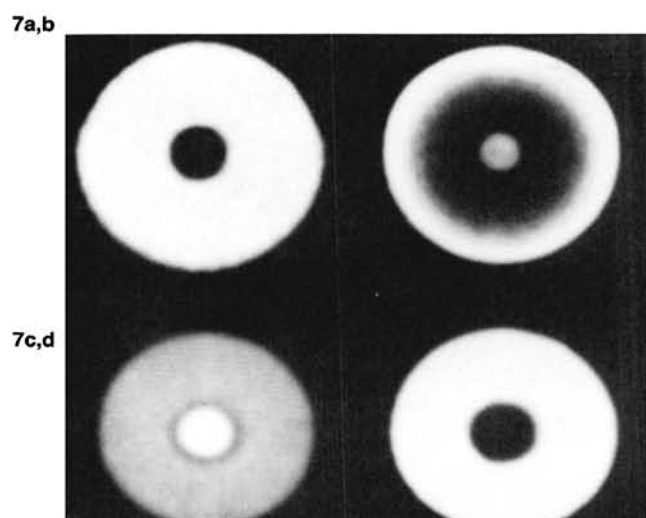
FIG. 7. "Donut" phantom with 4.5 cm diameter air pocket located in center. **(a)** Transmission image of the object; **(b)** emission image without attenuation correction; **(c)** emission image with analytic attenuation correction, and **(d)** emission image with measured transmission data used for attenuation correction.

far less attenuating medium, i.e., air, was actually present, and the analytic method overcorrected the data. When transmission data are used to attenuation-correct the data, however, a correct result is obtained.

Instrument Shielding

For the outermost straight-across plane and an empty port, the random and deadtime corrected co-incidence count rate due to a hot source outside the camera field of view was less than 93, 26, and 6 random and deadtime-corrected coincidence cps/mCi for a source positioned at 2.5, 15, and 30 cm from the center of the outermost ring. For the in-nermost straight-across plane, 9.2 cm inward from the first ring, these count rates were 42, 11, and 3 cps/mCi. Placing the head-like scattering medium in the port decreased the observed count rates by 4–22% for the outermost plane and 59–91% for the innermost plane. For a 25 mCi source just outside the outermost plane, approximately 2.2 kcps would thus result (these counts appear near the edge of the field of view in the reconstructed image). The empty-port background count rates were all less than 2 coincidence cps.

Image Quality

Figure 8a illustrates a transmission scan of the Derenzo phantom obtained using a high resolution CT scanner (Deltascan 2020). The corresponding PET image appears as Fig. 8b and contains approximately 133 million raw coincidence counts. The 3.5 mm hot spots are clearly distinguishable.

A high resolution CT scan of the cold spot phantom and its PET image appear in Fig. 9. The PET image was produced from approximately 444 million raw coincidence counts. The 6 mm cold spot is distinguishable both when it appears in a group and when it appears by itself. The 4 mm cold spot is also visible.

For the steady-state $CO^{15}O$ study (10 mCi/L continuous inhalation at 0.4 L/min), count rates of
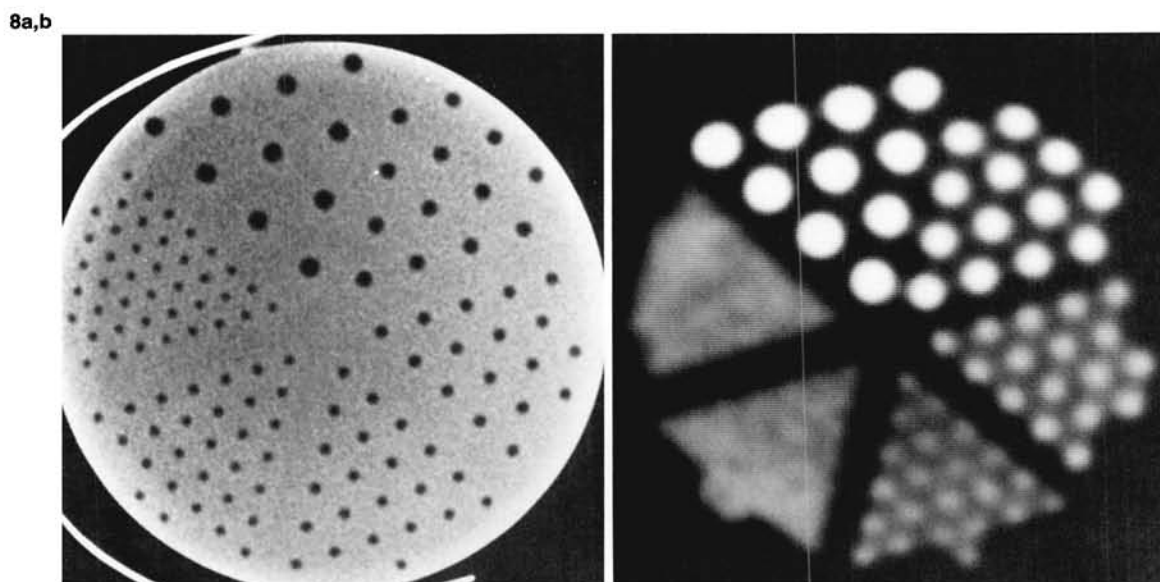

FIG. 8. The Derenzo hot spot phantom. **(a)** High resolution CT scan; **(b)** PET image.
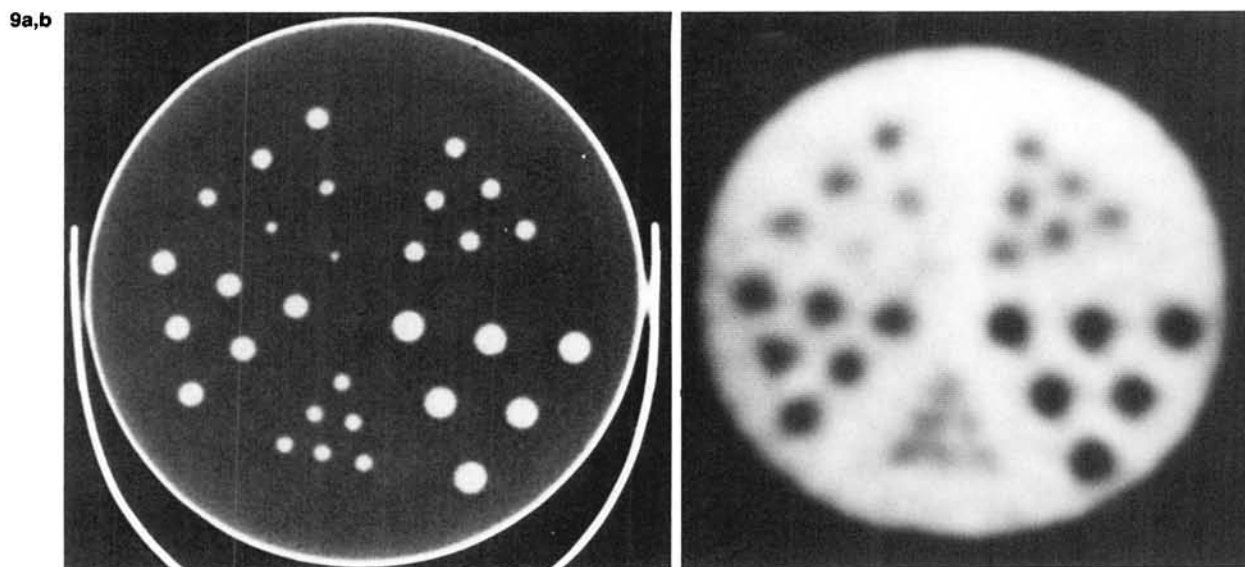
9a,b

FIG. 9. Cold spot phantom. (a) High resolution CT scan; (b) PET image.

1,900 raw coincidence cps were attained in a 1 cm slice at the level of the fourth ventricle. The dynamic capability of the PC 4600 is apparent in Fig. 10a, showing the approach to equilibrium of a small (9 cc) gray matter region. The high resolution steady-state image, with 1.5 million raw coincidence counts, appears as Fig. 10b. The basal ganglia, thalamus, and external capsule are clearly delineated in this 1 cm thick tomogram, obtained at the level of the third ventricle.

Maps of cerebral blood volume in a normal human subject appear in Fig. 11 at four separate levels of the brain. The circle of Willis and other cerebrovascular structures are clearly distinguish-

able in these images, which contain 0.3 to 1.3 million raw coincidence counts.

CONCLUSIONS

Overall, the performance characteristics of the PC 4600 are consistent with the requirements of our experimental program. The underlying design concept favors contiguous, multislice data acquisition and provides nearly uniform resolution over the field of view, both axially and in the transverse plane. Cross-plane axial resolution uniformity is a
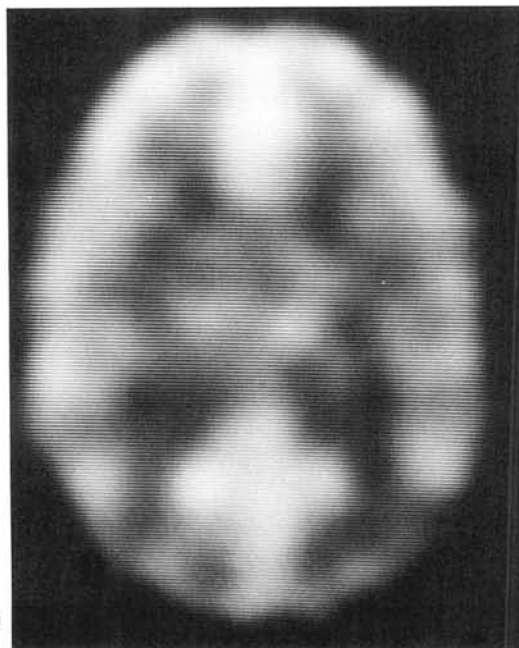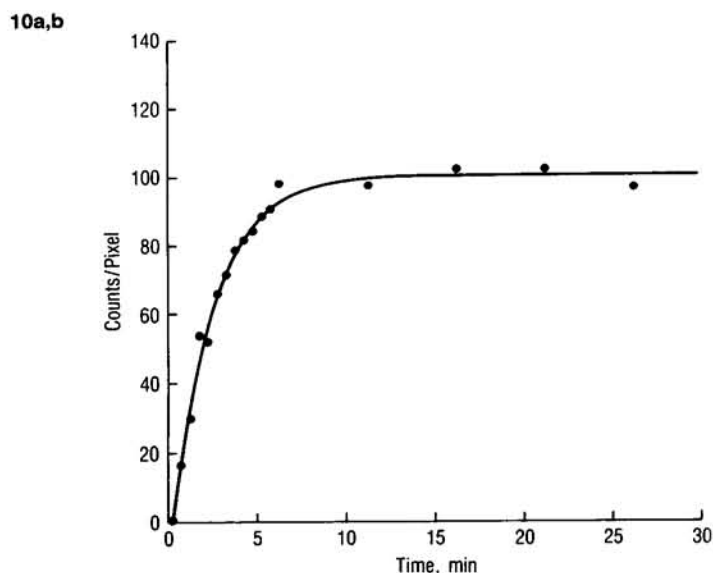
10a,b

FIG. 10. (a) Approach to equilibrium in a 9.25 cc region of gray matter during continuous inhalation of $CO^{15}O$ by a normal human subject; (b) high resolution equilibrium $CO^{15}O$ image obtained at level of the third ventricle, containing approximately 1.5 million raw coincidence counts.
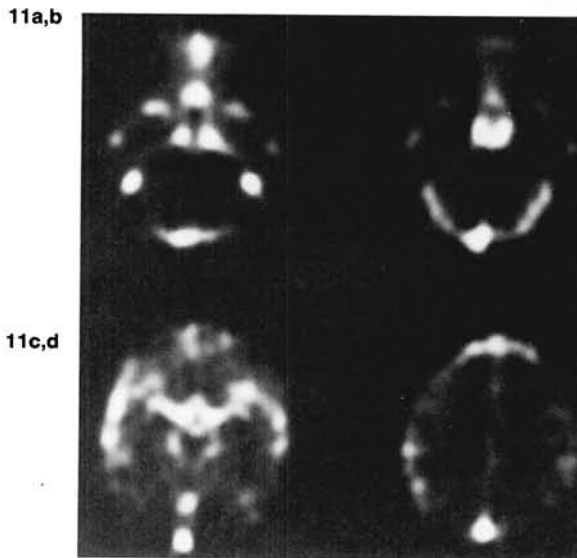
11a,b

11c,d

FIG. 11. Thin-slice images of normal human subject obtained following a bolus inhalation of ^{11}CO at four brain levels: **(a)** 0.8 million counts, **(b)** 1.3 million counts; **(c)** 0.9 million counts, **(d)** 0.3 million counts.

substantial benefit which allows the multislice quantitative capability to be fully exploited. The unique ORS provides a method for obtaining experimental attenuation data that is potentially superior to other techniques. The rapid-scan, multiplane data acquisition system is complemented by high-speed reconstruction and other processing software and hardware aids, all of which make the PC 4600 Neuro-PET an instrument of great clinical potential.

REFERENCES

1. Brownell GL, Sweet WH. Localization of brain tumors with positron emitters. *Nucleonics* 1953;11:40–5.
2. Hoffman EJ, Phelps ME, Mullani NA, Higgins CS, Ter-Pogossian MM. Design and performance characteristics of a whole-body positron transaxial tomograph. *J Nucl Med* 1976;17:493–502.
3. Cho ZH, Cohen MB, Singh M, Erikssen L, Chan J, MacDonald N, Spolter L. Performance and evaluation of the circular ring transverse axial positron camera (CRTAPC). *IEEE Trans Nucl Sci* 1977;NS-24:532–43.
4. Bohm C, Eriksson L, Bergström M, Litton J, Sunerman R. A computed assisted ring detector positron camera system for reconstruction tomography of the brain. *IEEE Trans Nucl Sci* 1978;NS-25:624–37.
5. Carroll LR. Design and performance characteristics of a production model positron imaging system. *IEEE Trans Nucl Sci* 1978;NS-25:606–14.
6. Phelps ME, Hoffman EJ, Huang SC, Kuhl DE. ECAT: a new computerized tomographic imaging system for positron-emitting radiopharmaceuticals. *J Nucl Med* 1978;19:635–47.
7. Ter-Pogossian MM, Mullani WA, Hood JT, Higgins JS, Currie

CM. A multi-slice positron emission computed tomograph (PETT IV) yielding transverse and longitudinal images. *Radiology* 1978;128:477–84.
8. Ter-Pogossian MM, Mullani WA, Hood JT, Higgins CY, Ficke DC. Design considerations for a positron emission transverse tomograph (PETT V) for the imaging of the brain. *J Comput Assist Tomogr* 1978;2:539–44.
9. Thompson CJ, Yamamoto YL, Meyer E. Positome II, a high-efficiency PET device for dynamic studies. *J Comput Assist Tomogr* 1978;2:650–1.
10. Brownell G, Burnham C, Correia J, Chesler D, Ackerman R, Taveras J. Transverse section imaging with the MGH positron camera. *IEEE Trans Nucl Sci* 1979;NS-26:2698–702.
11. Derenzo SE, Budinger TF, Cahoon JL, Greenberg WL, Huesman RH, Vuletich T. The Donner 280-crystal high-resolution positron tomograph. *IEEE Trans Nucl Sci* 1979;NS-26:2790–3.
12. Williams CW, Crabtree MC, Burgiss SG. Design and performance characteristics of a positron emission computed axial tomograph—ECAT-II. *IEEE Trans Nucl Sci* 1979;NS-26:619–27.
13. Nahara N, Tanaka E, Tomitani T, Yamamoto M, Murayama H, Suda Y, Endo M, Jinuma T, Tateno Y, Shishido F, Ishimaturu K, Ueda K, Takami K. Positologia: a positron ECT device with a continuously rotating detector ring. *IEEE Trans Nucl Sci* 1980;NS-27:1128–36.
14. Brooks RA, Sank VJ, Friauf WS, Leighton SB, Cascio HE, Di Chiro G. Design considerations for positron emission tomography. *IEEE Trans Biomed Eng* 1981;BME-28:158–77.
15. Kanno I, Uemura K, Miura S, Miura Y. HEADTOME: a hybrid emission tomograph for single photon and positron emission imaging of the brain. *J Comput Assist Tomogr* 1981;5:216–26.
16. Ter-Pogossian MM, Ficke DC, Hood JT Sr, Yamamoto M, Mullani NA. PETT VI: a positron emission tomograph utilizing cesium fluoride scintillation detectors. *J Comput Assist Tomogr* 1982;6:125–33.
17. Carroll LR, Hendry GO, Currin JD. Design criteria for multislice positron emission computed tomography detection systems. *IEEE Trans Nucl Sci* 1980;NS-27:485–8.
18. King PH, Hubner K, Gibbs W, Holloway E. Noise identification and removal in positron imaging systems. *IEEE Trans Nucl Sci* 1981;NS-28:148–51.
19. Bergström M, Eriksson L, Bohm C, Blomqvist G, Litton J. Correction for scattered radiation in a ring detector positron camera by integral transformation of the projections. *J Comput Assist Tomogr* 1983;7:42–50.
20. Logan J, Bernstein HJ. A Monte Carlo simulation of Compton scattering in positron emission tomography. *J Comput Assist Tomogr* 1983;7:316–20.
21. Carroll LR, Kretz P, Orcut G. The orbiting rod source: improving performance in PET transmission correction scans. In: Esser PD, ed. *Emission computed tomography—current trends.* New York: Society of Nuclear Medicine, 1983.
22. Brooks RA, Sank VJ. Comments on specifying the performance of a positron tomograph. *J Nucl Med* 1982;23:942.
23. Links JM, Wagner HR. Specification of performance of positron emission tomography scanners. *J Nucl Med* 1982; 23:82.
24. Marquardt DW. An algorithm for least-squares estimation of nonlinear parameters. *J Soc Indust Appl Math* 1963;11:431–41.
25. Eichling JO, Higgins CS, Ter-Pogossian MM. Determination of radionuclide concentrations with positron CT scanning (PETT): concise communication. *J Nucl Med* 1977;18:845–7.
26. Hoffman EJ, Phelps ME, Huang S-C, Plummer P, Kuhl DE. Evaluating the performance of multiple positron tomographs designed for brain imaging. *IEEE Trans Nucl Sci* 1982;NS-29:469–73.
27. Derenzo SE, Budinger TF, Cahoon JL, Huesman RH, Jackson HG. High resolution computed tomography of positron emitters. *IEEE Trans Nucl Sci* 1977;NS-24:544–58.